

ARTICLE OPEN

Body-centered-cubic structure and weak anharmonic phonon scattering in tungsten

Yani Chen^{1,2}, Jinlong Ma¹, Shihao Wen¹ and Wu Li^{1*}

It was recently found that the anharmonic phonon–phonon scattering in tungsten is extremely weak at high frequencies, leading to a predominance of electron–phonon scattering and consequently anomalous phonon transport behaviors. In this work, we calculate the phonon linewidths of W along high-symmetry directions from first principles. We find that the weak phonon–phonon scattering can be traced back to two factors. The first is the triple degeneracy of the phonon branches at the P and H points, a universal property of elemental body-centered-cubic (bcc) structures. The second is a relatively isotropic character of the phonon dispersions. When both are met, phonon–phonon scattering rates must vanish at the P and H points. The weak phonon–phonon scattering feature is also applicable to Mo and Cr. However, in other elemental bcc substances like Na, the isotropy condition is violated due to the unusually soft character of the lower transverse acoustic phonon branch along the Γ -N direction, opening emission channels and leading to much stronger phonon–phonon scattering. We also look into the distributions of electron mean-free paths (MFPs) at room temperature in tungsten, which can help engineer the resistivity of nanostructured W for applications such as interconnects.

npj Computational Materials (2019)5:98

; <https://doi.org/10.1038/s41524-019-0235-7>

INTRODUCTION

It is widely accepted that, around and above room temperature, electron–phonon coupling in metals has a much weaker effect on phonon scattering than anharmonic phonon–phonon interactions.¹ This has been verified for some common metals (Al, Ag, Au, Cu, Pt, and Ni) using first-principles techniques.^{2,3} However, NbC and W have been identified as exceptions by very recent calculations.^{4,5} In those materials, electron–phonon scattering is comparable to or stronger than phonon–phonon scattering, leading to an anomalously weak temperature dependence of the lattice thermal conductivity (κ_{ph}). Likewise, the unusual temperature dependence of κ_{ph} in NbSe₃ nanowires below the charge-density-wave transition temperature was found to be related to electron–phonon coupling.⁶ A common feature of these systems is a significant κ_{ph} ; specifically, κ_{ph} reaches as much as 46 W/m-K in W .⁵ The situation is reminiscent of heavily doped Si, where electron–phonon scattering can also be comparable to phonon–phonon scattering. When the carrier density reaches $1 \times 10^{21} \text{ cm}^{-3}$, electron–phonon scattering can lead to a reduction of κ_{ph} by 45% in Si.⁷

It is difficult, without assuming a value for the Lorenz number, to decouple the lattice and electronic contributions to the thermal conductivity in experimental measurements. The phonon linewidths are the most critical intermediate physical quantities of determining κ_{ph} . These linewidths are accessible to measurement techniques, such as inelastic neutron scattering or X-ray scattering, and can therefore provide direct verification of theoretical calculations. Other related quantities include the electron–phonon enhancement of electron mass, the electron–phonon spectral function α^2F , the electrical conductivity (σ), the electronic thermal conductivity, and the superconducting transition temperature.

In this paper, we quantify the contributions to the phonon linewidths of W due to electron–phonon and phonon–phonon interactions from first principles. We attribute the weak phonon–phonon scattering at high frequencies, crucial for its

anomalous phonon transport properties,⁵ to the elemental body-centered-cubic (bcc) structure, in which phonon frequencies are triply degenerated at the high-symmetry P and H points. We further use the example of Na, of which the phonon dispersions display unusually strong anisotropy, to illustrate that the bcc structure is a necessary but not sufficient condition to guarantee the weak phonon–phonon scattering. We also study α^2F and the mean-free path (MFP) distributions of electrons and phonons for W , relevant to size effects in applications such as nano-interconnects.^{8–11} Furthermore, we assess the accuracy of Allen's approximation to calculate the resistivity.

RESULTS AND DISCUSSION

 W and Mo

The calculated phonon dispersions and the contributions to the phonon full-width at half maximum (FWHM) for W from anharmonic phonon–phonon scattering at $T=0 \text{ K}$ and $T=300 \text{ K}$, from electron–phonon interactions and from isotope scattering, along the same high-symmetry path, are plotted in Fig. 1. Note that the longitudinal acoustic (LA) branch comprises the lowest-frequency modes along the P-H segment. The two transverse acoustic (TA) branches are degenerate along Γ -P-H- Γ . At the P and H points, all three branches are degenerate as a result of the space-group symmetry of elemental bcc structures, a point that we will explain in more detail in Section “Symmetry analysis for the triple degeneracy at the P and H points”. The linewidths are also the same for these degenerate branches. Isotope scattering is negligible compared to phonon–phonon and electron–phonon scattering.

As expressed in Eq. (2), the contribution to the FWHM from anharmonic phonon–phonon scattering Γ^{PP} is determined by the equilibrium phonon occupancies, the phase space available for scattering, and the scattering matrix elements V . For the three-phonon scattering processes $\lambda + \lambda' \rightleftharpoons \lambda''$, where a phonon mode

¹Institute for Advanced Study, Shenzhen University, 518060 Shenzhen, China. ²Key Laboratory of Optoelectronic Devices and Systems of Ministry of Education and Guangdong Province, College of Optoelectronic Engineering, Shenzhen University, 518060 Shenzhen, China. *email: wu.li.phys2011@gmail.com

is denoted by a composite index λ comprising both a wavevector \mathbf{q} and a branch index p), conservation of energy and quasi-momentum requires that the phase velocity of λ'' be greater than at least of one of those for λ and λ' .¹ Therefore, for typical elemental materials in which the phonon dispersions are nearly isotropic and tend to a horizontal tangent at the zone boundary, λ'' must lie in a branch higher than λ or λ' .¹ The lowest-lying branch phonons are prevented from emission, while the highest-lying branch phonons are prevented from absorption.

At 0 K, all lattice modes are unexcited. Since the contributions to Γ^{PP} from absorption processes are proportional to $n_{\lambda}^0 - n_{\lambda'}^0$, they are all zero in this 0 K limit, and the only nonzero contributions come from emission processes. Since the phonon dispersions of W can be described as typical with respect to the features mentioned in the previous paragraph, phonons lying on the lowest-lying branch throughout the whole Brillouin zone, including the Γ -P-H- Γ -N path, have vanishing Γ^{PP} at 0 K. The frequency differences between LA and TA modes are small along the P-H segment, and only a small number of emission processes are allowed for TA modes. The corresponding Γ^{PP} for the TA branches at 0 K are very small, but not strictly zero. The degeneracy of the TA modes is slightly lifted along the Γ -N segment. For similar reasons, the higher-lying TA branch along the Γ -N path has small but nonzero linewidths. There are many more emission channels for the LA modes, including $\text{LA} \rightarrow \text{TA} + \text{TA}$ and $\text{LA} \rightarrow \text{TA} + \text{LA}$ processes. The LA linewidth can therefore reach as high as 0.0045 THz at the N point [Fig. 1b].

An important feature of Γ^{PP} is that it always vanishes at the high-symmetry P and H points regardless of the temperature

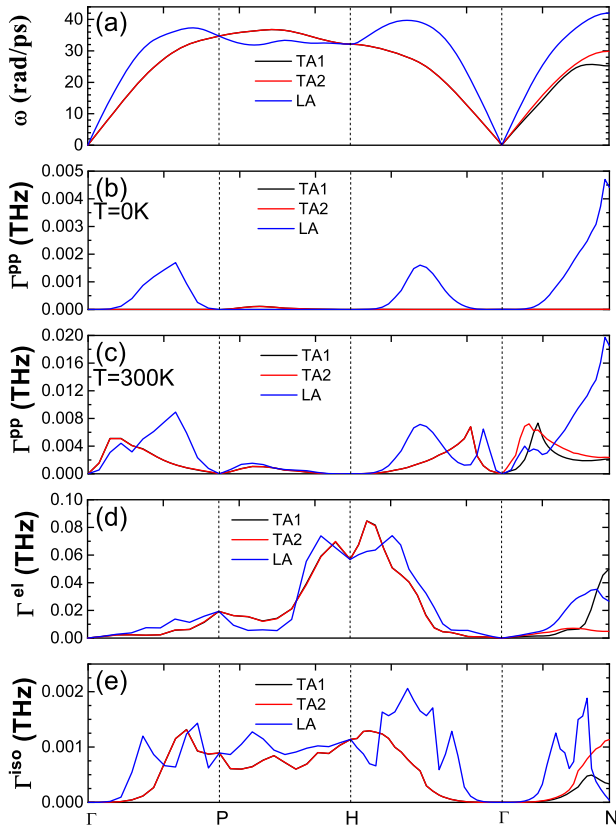


Fig. 1 Phonon dispersions (a) and contributions to the phonon full widths at half maximum for W along a high-symmetry path from anharmonic phonon–phonon scattering at $T = 0$ K (b) and $T = 300$ K (c), electron–phonon scattering (d) and isotope scattering (e). TA1, TA2, and LA denote the lower transverse acoustic, the higher transverse acoustic and the longitudinal acoustic branches, respectively

[Fig. 1b, c]. Although the phonon frequencies do not reach maxima at the P and H boundary points, the group velocities at those points are smaller than those of any branch in the neighborhood of the Γ point. As a result, absorption channels are still prevented by the restriction of energy and quasi-momentum conservation. At any other point different from P or H, a phonon lying on a lower branch can be always scattered to a higher branch by absorbing a phonon. For instance, at the N point, $\text{TA} + \text{TA/LA} \rightarrow \text{LA}$ channels are always allowed.

Electron–phonon scattering is much weaker than anharmonic phonon–phonon scattering at the zone center. However, it dominates over the latter close to the zone boundary, mainly due to the weakness of phonon–phonon scattering, which vanishes at the P and H points. The contribution to the FWHM from electron–phonon scattering Γ^{el} reaches a maximum value of over 0.08 THz around the H point. This unusual predominance of Γ^{el} at high frequencies leads to anomalous phonon transport behaviors.^{4,5} Γ^{el} is temperature independent, whereas above room temperature Γ^{ph} is approximately proportional to T . This is easy to understand since the Debye temperature of W (383 K) is only slightly higher than room temperature.¹² Note that anharmonic phonon–phonon scattering, as calculated here, is limited to three-phonon processes. Considering higher orders would increase the FWHM slightly.¹³ Additionally, the total FWHMs at P and H points will display weak temperature dependence.

The feature of weak phonon–phonon scattering is not unique to the individual bcc substance W . We have also studied another elemental bcc system Mo. The phonon dispersions of Mo are plotted in Fig. 2a. The phonon dispersion shape of Mo looks rather similar to that of W . Γ^{PP} is also zero at P and H points [Fig. 2b, c]. Furthermore, the frequency differences between the LA and TA modes along the P-H path are even smaller than in W . As a result, the phonon scattering rates between P and H are smaller and almost vanishing even at $T = 300$ K. Considering that chromium also has similar phonon dispersions,¹⁴ it can be expected to also share this feature.

Just like the vanishing Γ^{PP} at P and H, the exponent of the power-law dependence of the acoustic phonon lifetimes on q at low temperatures and close to the zone center depends on the crystal structure, as pointed out by Herring.¹⁵ However, as demonstrated recently for the cases of GaAs¹⁶ and Si,¹⁷ this asymptotic power-law dependence can and does break down further away from the zone center, due to the interplay between Herring and non-Herring phonon–phonon processes. Note that

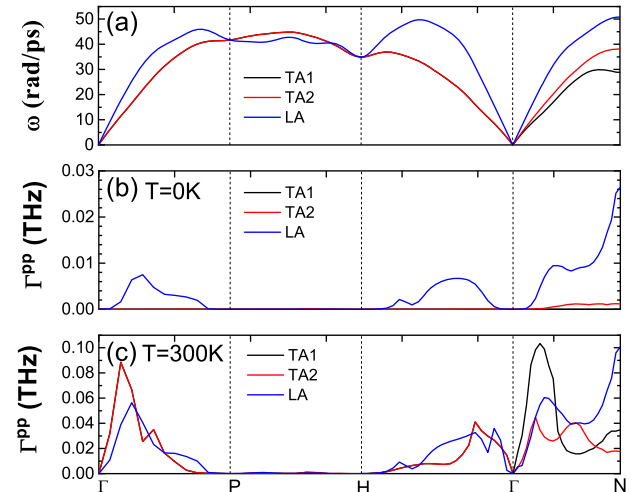


Fig. 2 Phonon dispersions (a) and contributions to the phonon full widths at half maximum for Mo along a high-symmetry path from anharmonic phonon–phonon scattering at $T = 0$ K (b), and $T = 300$ K (c). TA1, TA2, and LA follow the same notations as in Fig. 1

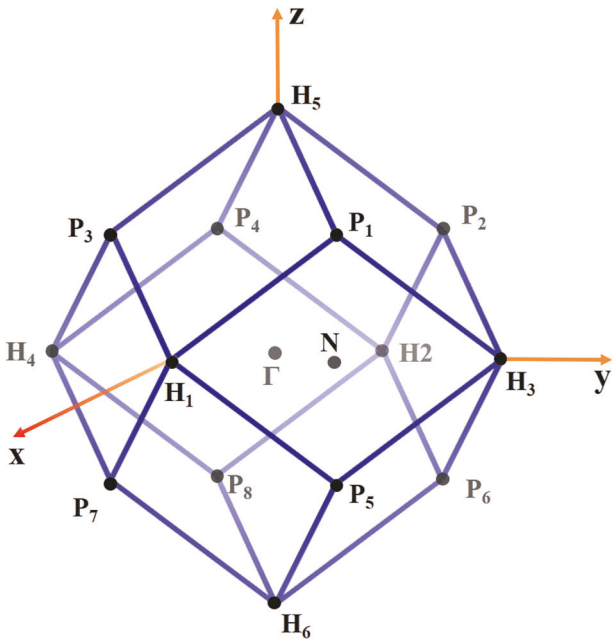


Fig. 3 The Brillouin zone of a body-centered-cubic structure with some high-symmetry points labeled. Only a single representative N point is labeled. The Cartesian coordinates of these points in units of $2\pi/a$ are $N = (0.5, 0.5, 0)$, $H_1 = (1, 0, 0)$, $H_2 = (-1, 0, 0)$, $H_3 = (0, 1, 0)$, $H_4 = (0, -1, 0)$, $H_5 = (0, 0, 1)$, $H_6 = (0, 0, -1)$, $P_1 = (0.5, 0.5, 0.5)$, $P_2 = (-0.5, 0.5, 0.5)$, $P_3 = (0.5, -0.5, 0.5)$, $P_4 = (-0.5, -0.5, 0.5)$, $P_5 = (0.5, 0.5, -0.5)$, $P_6 = (-0.5, 0.5, -0.5)$, $P_7 = (0.5, -0.5, -0.5)$, $P_8 = (-0.5, -0.5, -0.5)$

the present work focuses on a phenomenon at the P and H points, which are located at the zone boundary, and is thus not directly connected to that universal behavior at the zone center.

Symmetry analysis for the triple degeneracy at the P and H points
As discussed above, the triple degeneracy of phonon frequencies at the P and H points is a crucial ingredient for the vanishing Γ^{PP} . This degeneracy is inherent in elemental bcc structures, which belong to the space-group $\text{Im}\bar{3}m$ (No. 229), so it is worth explaining its origin in more detail.

As shown in Fig. 3, there are six symmetry equivalent H points in the Brillouin zone, located along the three Cartesian axes in the figure. All those points are identical up to a translation by a certain reciprocal lattice vector. For any phonon wavevector \mathbf{q} along a given Γ -H direction, a rotation of 90° around Γ -H leaves both the structure and \mathbf{q} invariant; therefore, the two TA branches must be degenerate along the Γ -H direction. To show that LA is also degenerate with those two TA modes at H, we take the example of H_1 , a point at which the LA mode vibrates along the x -axis. The symmetry operation of rotating around the z -axis by 90° maps this LA mode to a vibration along the y -axis at H_3 . Since H_1 and H_3 are identical, the y direction vibration at H_3 is actually one TA mode at H_1 . This proves that the LA and TA branches must be degenerate at H_1 , and thus at each H point.

The case of P points is similar. There are eight symmetry equivalent P points in the Brillouin zone. If we restrict ourselves to translations by a reciprocal lattice vector, there are two equivalence classes, namely $\{P_1, P_4, P_6, P_7\}$ and $\{P_2, P_3, P_5, P_8\}$, following the notation of Fig. 3. For any \mathbf{q} along a particular Γ -P direction, the symmetry operation of rotating around this axis by 120° can mix up the two TA modes. Those are thus required to be degenerate along the Γ -P direction. At P_1 the LA mode vibrates along the $\hat{x} + \hat{y} + \hat{z}$ direction. The symmetry operation of rotating

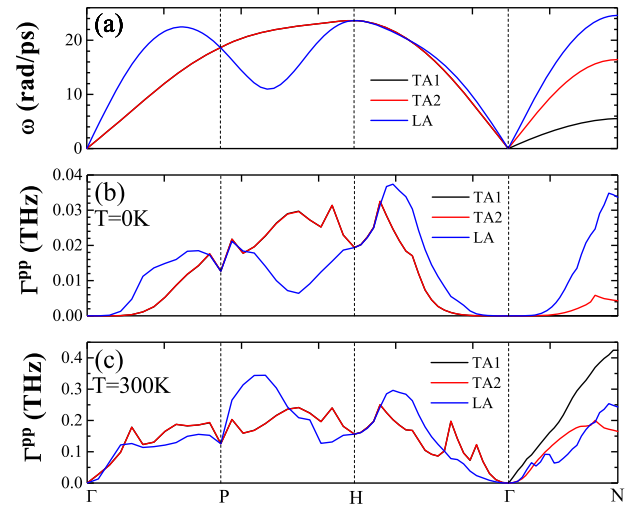


Fig. 4 Phonon dispersions (a) and contributions to the phonon full widths at half maximum for Na along a high-symmetry path from anharmonic -phonon scattering at $T = 0\text{ K}$ (b) and $T = 300\text{ K}$ (c). TA1, TA2, and LA follow the same notations as in Fig. 1

around the z -axis by 180° will transform this mode into a vibration along the $-\hat{x} - \hat{y} + \hat{z}$ direction at P_4 . The latter actually corresponds to a certain superposition of the TA and LA modes at P_1 , since P_1 and P_4 are identical. Therefore, the LA and TA modes should be degenerate at P_1 and any P point.

Systems with soft phonons: the case of Na

In spite of its importance as a necessary condition, the triple degeneracy of phonon frequencies at the P and H points shared by all elemental bcc systems is not sufficient to guarantee that Γ^{PP} vanishes there. We illustrate this by studying the case of Na. The phonon dispersions of Na are plotted in Fig. 4a, and display strong anisotropy, particularly for the TA modes. The lower TA branches are unusually soft along the Γ -N direction as compared to other directions, consistent with a bcc-hcp structural phase transition.¹⁸ This makes a huge difference in terms of phase space for three-phonon scattering: in contrast to the cases of W and Mo , where the emission channels for the lowest-lying branches are completely forbidden, the lowest-lying phonons with wavevectors from other directions of the Brillouin zone can easily emit a phonon lying in the lower TA branch along the Γ -N direction. As a result [see Fig. 4b], Γ^{PP} at 0 K, which only involves contributions from emission processes, has large nonzero values for the lowest-lying branches everywhere except along the Γ -N path. At 300 K, Γ^{PP} is very large for the lowest-lying branch along the Γ -N path [Fig. 4c], due to numerous allowed absorption processes, each one the inverse of an emission process. Given the fact that the group velocities at P are larger than those for the lower-lying TA branch along the Γ -N direction, the absorption channels are also opened at P. However, absorption processes are forbidden at H. We note that many other bcc elemental substances, including Li, K, Rb, Cs,¹⁹ Ba²⁰, and Ta²¹ also possess soft phonons along the Γ -N direction, and therefore Γ^{PP} is expected to be similarly strong in those systems.

Electrical transport and MFPs of electrons and phonons in W
Moving on to electrical transport, our calculated Eliashberg electron-phonon spectral function α^2F and its transport variant α^2F_{tr} are plotted in Fig. 5 and lead to values of 0.29 and 0.28 for total electron-phonon coupling constant λ and its transport counterpart λ_{tr} , respectively. Our value of λ is slightly larger than the literature value of 0.28, which was obtained based on

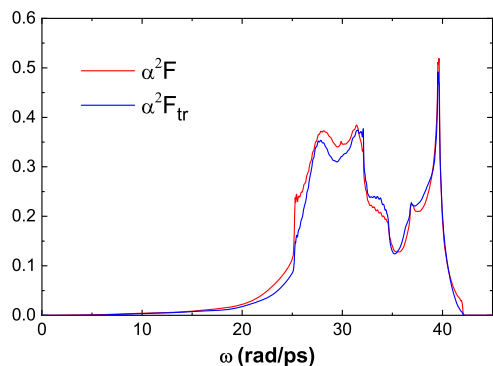


Fig. 5 Eliashberg electron–phonon spectral function α^2F and its transport variant α^2F_{tr} for W

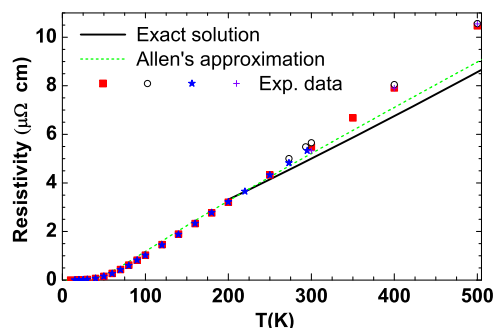


Fig. 6 Resistivity of W calculated from the exact solution⁵ (solid line), and Allen's approximation (dotted line) to the BTE. The symbols denote experimental electrical resistivity values taken from ref.⁴⁶

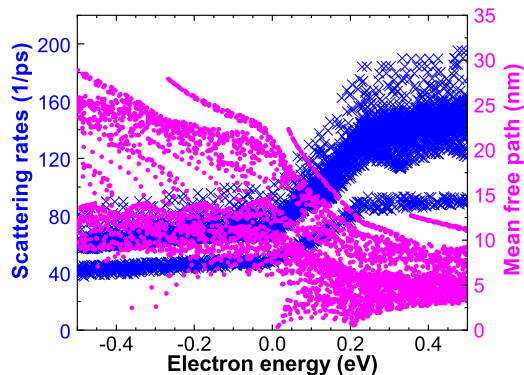


Fig. 7 Room-temperature electron scattering rates and mean-free paths vs. energy (relative to E_f) for W

estimates^{22,23} or first-principles calculations.²⁴ The resistivity afforded by Eq. (7) is plotted in Fig. 6. It slightly overestimates the exact solution, which was obtained by solving the BTE iteratively,^{5,25} only by up to 5% at 500 K. Both Allen's approximation and the exact solution to the BTE underestimate the measured resistivity, especially at higher temperatures.⁵

When the temperature is higher than the Debye temperature, the average scattering rate of electrons can be obtained from Allen's approximation²⁶

$$\overline{\tau}^{-1} = \frac{2\pi}{\hbar} k_B T \lambda. \quad (1)$$

Its value at room temperature for W is 72 ps^{-1} , which falls in the middle of the actual distribution of scattering rates⁵ [Fig. 7] and is consistent with the lifetime (16 fs) estimated from the measured ρ and the calculated band structure in ref.⁸. The scattering rates

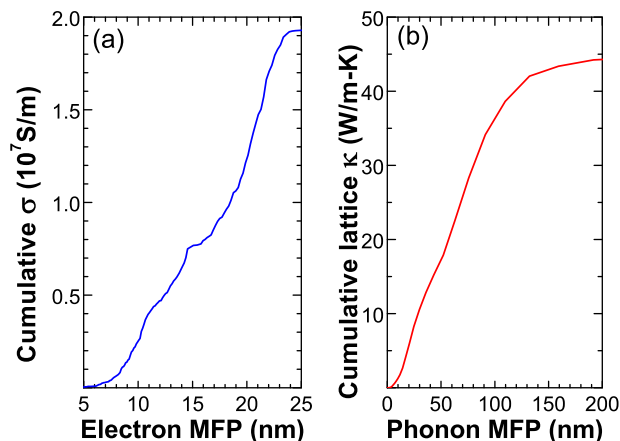


Fig. 8 Cumulative electrical conductivity vs. electron mean-free path **a** and cumulative lattice thermal conductivity vs. phonon mean-free path **b** at room temperature for W

span a factor of 2, which renders some support to the constant lifetime assumed in ref.⁸.

Because of the boundary contribution to scattering, the ρ of metal wires is higher than the bulk value once entering the nanoscale. Moreover, the relative increase is material-dependent, so it is possible to find a metal that is more resistive than copper in the bulk, but whose wires have lower ρ than copper wires of the same size. In fact, finding such metal nanowires to replace copper nanowires as interconnect material is a major issue for the semiconductor industry.⁸ Likewise, grain boundary scattering is another source of size effects in polycrystals.^{27,28} A qualitative way to understand those size effects for a particular material is to look at the distribution of electron MFPs and their contributions to the conductivity.⁵ As shown in Fig. 7, the largest MFP is 24 nm at the Fermi level. According to the cumulative σ presented in Fig. 8a, the MFPs are distributed in the range from 5 nm to 24 nm at room temperature, and half of σ is contributed by electrons with MFPs shorter than 18 nm. The reported average MFP in the literature ranges from 254 nm.^{8,10,29–33} Specifically, our calculations are in consistent with ref.⁸, which estimated an average of 15.5 nm from the measured ρ and calculated band structure.

In contrast, phonons have longer MFPs than electrons in W . Ninety-percent of the κ_{ph} ⁵ is contributed by phonons with MFPs between 5 and 130 nm [Fig. 8b]. W has smaller electron MFPs and larger phonon MFPs than Al, Ag, and Au, which possess larger σ but much smaller κ_{ph} than W .² In those three metals, phonons with MFPs between 1 and 10 nm are the predominant contributors to κ_{ph} .² However, it should be noted that longer MFPs do not always imply higher conductivity: for instance, Al has almost the same σ as Au, but its average electron MFP is only half of that for Au.⁸ When the size is comparable to the characteristic MFPs, the transport properties are affected by the system size. In that regard, and since in W the MFPs of phonons are several times longer than those of electrons, size effects will result in a reduction of κ_{ph} for significantly larger sizes than needed to cause a reduction in σ . Therefore W nanostructures can be expected to show reduced values of the Lorenz number.⁵

In summary, we report the phonon linewidths of tungsten contributed from electron–phonon and phonon–phonon interactions along high-symmetry paths, calculated through first-principles techniques. The electron–phonon scattering dominates except in a neighborhood of the zone center. The unusually weak phonon–phonon scattering, and in particular its vanishing strength at the triply degenerate P and H points, can be traced back to the elemental bcc structure. Although this feature is also applicable to Mo and Cr, it is not a universal phenomenon common to all

elemental bcc substances. We find that in other systems like Na, the phonon–phonon scattering is strong due to the unusually soft transverse acoustic phonon along the Γ -N direction.

The electrical resistivity of W obtained with Allen’s approximation agrees well with the accurate solution to the linearized Boltzmann transport equation. The room temperature mean-free paths of electrons contributing to the conductivity range from 5 to 24 nm, much shorter than those of phonons, suggesting reduced Lorenz numbers in W nanostructures.

METHODS

The phonon FWHM corresponds to the scattering rate (inverse of the lifetime) divided by 2π . For a given mode denoted by λ (a composite index comprising both a wavevector \mathbf{q} and a branch index p) the FWHM due to anharmonic phonon–phonon scattering can be calculated as^{34,35}

$$\Gamma_{\lambda}^{\text{pp}} = \frac{\hbar}{8N_{\mathbf{q}}} \left[\sum_{\lambda'p'} (n_{\lambda'}^0 - n_{\lambda''}^0) \frac{\delta(\omega_{\lambda} + \omega_{\lambda'} - \omega_{\lambda''})}{\omega_{\lambda}\omega_{\lambda'}\omega_{\lambda''}} |V_{\lambda\lambda'\lambda''}^+|^2 + \frac{1}{2} \sum_{\lambda'p'} (n_{\lambda'}^0 + n_{\lambda''}^0 + 1) \frac{\delta(\omega_{\lambda} - \omega_{\lambda'} - \omega_{\lambda''})}{\omega_{\lambda}\omega_{\lambda'}\omega_{\lambda''}} |V_{\lambda\lambda'\lambda''}^-|^2 \right], \quad (2)$$

where $N_{\mathbf{q}}$ is the number of uniformly sampled \mathbf{q} points in the Brillouin zone, and n_{λ}^0 is the Bose–Einstein occupancy for phonon frequency ω_{λ} . There are two types of three-phonon processes: absorption (+) and emission (–) processes. The phonon of interest λ is scattered into phonon λ'' by absorbing/emitting phonon λ' in the absorption/emission process, also termed as coalescence/decay process in the literature.¹⁷ The conservation of quasi-momentum requires that $\mathbf{q}'' = \mathbf{q} \pm \mathbf{q}'$ up to a certain reciprocal lattice vector for the absorption and emission processes. The scattering matrix elements $V_{\lambda\lambda'\lambda''}^{\pm}$ are determined by the third-order interatomic force constants (IFCs).^{34,35}

The phonon FWHM due to isotopic mass disorder is given by³⁶

$$\Gamma_{\lambda}^{\text{iso}} = \frac{\omega_{\lambda}^2}{12} g_2 D(\omega_{\lambda}), \quad (3)$$

where $D(\omega)$ is phonon density of states per unit cell, and g_2 is the Pearson deviation coefficient of the atomic masses of isotopes. The natural isotopic distribution of W yields a value of g_2 of 6.9668×10^{-5} .

The contribution to the phonon FWHM from electron–phonon interactions is almost temperature independent, and can be well estimated as^{1,25}

$$\Gamma_{\lambda}^{\text{el}} = \omega_{\text{qp}} \sum_{\mathbf{k}} \frac{2}{N_{\mathbf{k}}} |g_{\mathbf{nk},\mathbf{qp}}^{m\mathbf{k}+\mathbf{q}}|^2 \delta(E_{m\mathbf{k}+\mathbf{q}} - E_F) \delta(E_{\mathbf{nk}} - E_F), \quad (4)$$

where $g_{\mathbf{nk},\mathbf{qp}}^{m\mathbf{k}+\mathbf{q}}$ is the electron–phonon coupling matrix element for the electron state with band index n and wavevector \mathbf{k} , the phonon mode (\mathbf{q} , p), and the electron state with band index m and wavevector $\mathbf{k} + \mathbf{q}$. $E_{\mathbf{nk}}$ and E_F are the corresponding electronic and Fermi energy, respectively. $N_{\mathbf{k}}$ is the number of uniformly sampled \mathbf{k} points in the Brillouin zone. The factor of 2 in $2/N_{\mathbf{k}}$ accounts for the spin degeneracy in non-spin-polarized calculations.

Γ^{el} is closely related to σ . Allen obtained an approximated solution to the Boltzmann transport equation (BTE) in metals, and related the electrical resistivity ρ to the transport spectral function $\alpha^2 F_{\text{tr}}$,²⁶ which is a variant of the Eliashberg electron–phonon spectral function $\alpha^2 F$. The latter can be written as³⁷

$$\alpha^2 F(\omega) = \frac{1}{2N_{\mathbf{q}}N_F} \sum_{\mathbf{qp}} \frac{\Gamma_{\mathbf{qp}}^{\text{el}}}{\omega_{\mathbf{qp}}} \delta(\omega - \omega_{\mathbf{qp}}), \quad (5)$$

where N_F is the electronic density of states per unit cell and per spin at the Fermi level E_F . The total coupling constant can be obtained as

$$\lambda = \frac{1}{N_{\mathbf{q}}} \sum_{\mathbf{qp}} \frac{\Gamma_{\mathbf{qp}}^{\text{el}}}{N_F \omega_{\mathbf{qp}}^2} = 2 \int d\omega \frac{\alpha^2 F(\omega)}{\omega}. \quad (6)$$

For transport properties, the contributions to scattering also depend on the effective change in velocity. Defining the efficiency factor α as

$$\alpha = 1 - \frac{\mathbf{v}_{m\mathbf{k}+\mathbf{q}} \cdot \mathbf{v}_{\mathbf{nk}}}{|\mathbf{v}_{\mathbf{nk}}|^2}, \quad (7)$$

and multiplying the term in the sum of Eq. (4) by α , one can obtain the transport analog of the spectral function $\alpha^2 F_{\text{tr}}$ and consequently the total

transport coupling constant λ_{tr} . The ρ of metals can be approximately obtained as:²⁶

$$\rho(T) = \frac{2\pi V k_B T}{e^2 \hbar N_F \langle v_z^2 \rangle} \int_0^{\infty} d\omega \frac{x^2}{\omega \sinh^2 x} \alpha^2 F_{\text{tr}}(\omega), \quad (8)$$

where V is the volume of the unit cell, $x = \hbar\omega/(2k_B T)$, and $\langle v_z^2 \rangle$ is the average square of the Fermi velocity along the transport direction, denoted here as z .

The electronic band structure, phonon dispersions and electron–phonon interactions were calculated using the QUANTUM ESPRESSO package,³⁸ combining density functional theory (DFT), and density functional perturbation theory (DFPT).³⁹ The Perdew–Zunger parametrization⁴⁰ of the local density approximation (LDA) and Bachelet–Hamann–Schlüter type norm-conserving pseudopotentials⁴¹ were used for W . The Perdew–Burke–Ernzerhof parametrization⁴² of the generalized gradient approximation (GGA) and Trouiller–Martins type norm-conserving Pseudopotentials were used for Mo and Na. The *thirdorder.py* script from the ShengBTE package³⁵ was used to generate the third-order IFCs⁴³ using $5 \times 5 \times 5$ supercells. The $\Gamma_{\lambda}^{\text{pp}}$ and $\Gamma_{\lambda}^{\text{iso}}$ were obtained on a $48 \times 48 \times 48$ \mathbf{q} grid by using the ShengBTE package.³⁵ Furthermore, the EPW package⁴⁴ was employed to perform Wannier function interpolation from initial $8 \times 8 \times 8$ \mathbf{k} and \mathbf{q} grids for the electron–phonon coupling matrix elements of W . The $\Gamma_{\lambda}^{\text{el}}$ were then obtained on $36 \times 36 \times 36$ \mathbf{k} and \mathbf{q} grids. The phonon and electron MFP analysis for W were carried out by solving the corresponding BTEs⁵ accurately with $36 \times 36 \times 36$ \mathbf{q} and $108 \times 108 \times 108$ \mathbf{k} grids, respectively. The δ -functions involved in Eqs. (2)–(5) are represented by Gaussian functions with physically motivated adaptive broadening parameters,^{25,45} eliminating the need for any adjustable parameters.

DATA AVAILABILITY

The data that support the findings of this study are available from the corresponding author upon reasonable request.

Received: 17 April 2019; Accepted: 11 September 2019;

Published online: 08 October 2019

REFERENCES

- Ziman, J. M. *Electrons and Phonons: The Theory of Transport Phenomena in Solids*. (Clarendon Press, London, 1960).
- Jain, A. & McGaughey, A. J. H. Thermal transport by phonons and electrons in aluminum, silver, and gold from first principles. *Phys. Rev. B* **93**, 081206 (2016).
- Wang, Y., Lu, Z. & Ruan, X. First principles calculation of lattice thermal conductivity of metals considering phonon-phonon and phonon-electron scattering. *J. Appl. Phys.* **119**, 225109 (2016).
- Li, C., Ravichandran, N. K., Lindsay, L. & Broido, D. Fermi surface nesting and phonon frequency gap drive anomalous thermal transport. *Phys. Rev. Lett.* **121**, 175901 (2018).
- Chen, Y., Ma, J. & Li, W. Understanding the thermal conductivity and Lorenz number in tungsten from first principles. *Phys. Rev. B* **99**, 020305 (R) (2019).
- Yang, L. et al. Distinct signatures of electron–phonon coupling observed in the lattice thermal conductivity of NbSe₃ nanowires. *Nano Lett.* **19**, 415 (2018).
- Liao, B. et al. Significant reduction of lattice thermal conductivity by the electron–phonon interaction in silicon with high carrier concentrations: a first-principles study. *Phys. Rev. Lett.* **114**, 115901 (2015).
- Gall, D. Electron mean free path in elemental metals. *J. Appl. Phys.* **119**, 085101 (2016).
- Zheng, P. & Gall, D. The anisotropic size effect of the electrical resistivity of metal thin films: Tungsten. *J. Appl. Phys.* **122**, 135301 (2017).
- Steinhögl, W. et al. Tungsten interconnects in the nano-scale regime. *Microelectron. Eng.* **82**, 266 (2005).
- Barako, M. T. et al. Quasi-ballistic electronic thermal conduction in metal inverse opals. *Nano Lett.* **16**, 2754 (2016).
- Tari, A. *The Specific Heat of Matter at Low Temperatures*. (Imperial College Press, London, 2003).
- Feng, T., Lindsay, L. & Ruan, X. Four-phonon scattering significantly reduces intrinsic thermal conductivity of solids. *Phys. Rev. B* **96**, 161201 (2017).
- Simonelli, G., Pasianot, R. & Savino, E. J. Phonon dispersion curves for transition metals within the embedded-atom and embedded-defect methods. *Phys. Rev. B* **55**, 5570 (1997).

15. Herring, C. Role of low-energy phonons in thermal conduction. *Phys. Rev.* **95**, 954 (1954).
16. Legrand, R., Huynh, A., Jusserand, B., Perrin, B. & Lemaître, A. Direct measurement of coherent subterahertz acoustic phonons mean free path in GaAs. *Phys. Rev. B* **93**, 184304 (2016).
17. Markov, M. et al. Breakdown of Herring's processes in cubic semiconductors for subterahertz longitudinal acoustic phonons. *Phys. Rev. B* **98**, 245201 (2018).
18. Xie, Y. et al. Origin of bcc to fcc phase transition under pressure in alkali metals. *New J. Phys.* **10**, 063022 (2008).
19. Wilson, R. B. & Riffe, D. M. An embedded-atom-method model for alkali-metal vibrations. *J. Phys.: Condens. Matter* **24**, 335401 (2012).
20. Mizuki, J., Chen, Y., Ho, K.-M. & Stassis, C. Phonon dispersion curves of bcc Ba. *Phys. Rev. B* **32**, 666 (1985).
21. Iizumi, M. Phonon dispersion relations of body-centered cubic thallium and the bcc-to-hcp martensitic phase transformation. *J. Phys. Soc. Jpn.* **52**, 549 (1983).
22. McMillan, W. L. Transition temperature of strong-coupled superconductors. *Phys. Rev.* **167**, 331 (1968).
23. Allen, P. B. & Dynes, R. C. Transition temperature of strong-coupled superconductors reanalyzed. *Phys. Rev. B* **12**, 905 (1975).
24. Daraszewicz, S. L. et al. Determination of the electron-phonon coupling constant in tungsten. *Appl. Phys. Lett.* **105**, 023112 (2014).
25. Li, W. Electrical transport limited by electron-phonon coupling from Boltzmann transport equation: An ab initio study of Si, Al, and MoS₂. *Phys. Rev. B* **92**, 075405 (2015).
26. Allen, P. B. New method for solving Boltzmann's equation for electrons in metals. *Phys. Rev. B* **17**, 3725 (1978).
27. César, M., Liu, D., Gall, D. & Guo, H. Calculated resistances of single grain boundaries in copper. *Phys. Rev. Appl.* **2**, 044007 (2014).
28. César, M., Gall, D. & Guo, H. Reducing grain-boundary resistivity of copper nanowires by doping. *Phys. Rev. Appl.* **5**, 054018 (2016).
29. Learn, A. J. & Foster, D. W. Resistivity, grain size, and impurity effects in chemically vapor-deposited tungsten films. *J. Appl. Phys.* **58**, 2001 (1985).
30. Mikhailov, G. M., Chernykh, A. V. & Petrashov, V. T. Electrical properties of epitaxial tungsten films grown by laser ablation deposition. *J. Appl. Phys.* **80**, 948 (1996).
31. Rossnagel, S. M., Noyan, I. C. & Cabral, C. Phase transformation of thin sputter-deposited tungsten films at room temperature, *Journal of Vacuum Science & Technology B: Microelectronics and Nanometer Structures Processing. Meas., Phenom.* **20**, 2047 (2002).
32. Choi, D. et al. Phase, grain structure, stress, and resistivity of sputter-deposited tungsten films. *J. Vac. Sci. Technol. A* **29**, 051512 (2011).
33. Choi, D. et al. Electron mean free path of tungsten and the electrical resistivity of epitaxial (110) tungsten films. *Phys. Rev. B* **86**, 045432 (2012).
34. Ward, A., Broido, D. A., Stewart, D. A. & Deinzer, G. Ab initio theory of the lattice thermal conductivity in diamond. *Phys. Rev. B* **80**, 125203 (2009).
35. Li, W., Carrete, J., Katcho, N. A. & Mingo, N. ShengBTE: a solver of the Boltzmann transport equation for phonons. *Comput. Phys. Commun.* **185**, 1747 (2014).
36. Tamura, S.-i Isotope scattering of dispersive phonons in Ge. *Phys. Rev. B* **27**, 858 (1983).
37. Allen, P. B. Neutron spectroscopy of superconductors. *Phys. Rev. B* **6**, 2577 (1972).
38. Giannozzi, P. et al. QUANTUM ESPRESSO: a modular and open-source software project for quantum simulations of materials. *J. Phys.: Condens. Matter* **21**, 395502 (2009).
39. Baroni, S., de Gironcoli, S., Dal Corso, A. & Giannozzi, P. Phonons and related crystal properties from density-functional perturbation theory. *Rev. Mod. Phys.* **73**, 515 (2001).
40. Perdew, J. P. & Zunger, A. Self-interaction correction to density-functional approximations for many-electron systems. *Phys. Rev. B* **23**, 5048 (1981).
41. Bachelet, G. B., Hamann, D. R. & Schlüter, M. Pseudopotentials that work: From H to Pu. *Phys. Rev. B* **26**, 4199 (1982).
42. Perdew, J. P., Burke, K. & Ernzerhof, M. Generalized gradient approximation made simple. *Phys. Rev. Lett.* **77**, 3865 (1996).
43. Li, W., Lindsay, L., Broido, D. A., Stewart, D. A. & Mingo, N. Thermal conductivity of bulk and nanowire Mg₂Si_xSn_{1-x} alloys from first principles. *Phys. Rev. B* **86**, 174307 (2012).
44. Poncé, S., Margine, E., Verdi, C. & Giustino, F. EPW: electron-phonon coupling, transport and superconducting properties using maximally localized Wannier functions. *Comput. Phys. Commun.* **209**, 116 (2016).
45. Li, W. et al. Thermal conductivity of diamond nanowires from first principles. *Phys. Rev. B* **85**, 195436 (2012b).
46. Hellwege, K.-H. and Madelung, O (eds) Metals: electronic transport phenomena: electrical resistivity, Kondo and spin fluctuation systems, spin glasses and thermopower, in *Landolt-Börnstein, Group III, New Series, Vol. 15a* (Springer, Berlin, 1982).

ACKNOWLEDGEMENTS

We acknowledge support from the Natural Science Foundation of China (NSFC) under Grants No. 11704258 and No. 11574198 and the Shenzhen Science, Technology and Innovation Commission under Grant No. JCYJ20170412105922384. Y.C. also acknowledges the support from the China Postdoctoral Science Foundation under Grant No.2017M622745. J.M. also acknowledges support from NSFC under Grant No. 11804229. We thank Dr. Jesús Carrete for his critical reading of the manuscript.

AUTHOR CONTRIBUTIONS

Y.C. performed calculations for W and Na. S.W. performed calculations for Mo. J.M. wrote the code. W.L. conceived the project. All authors contributed to the data analysis and wrote the paper.

COMPETING INTERESTS

The authors declare no competing interests.

ADDITIONAL INFORMATION

Correspondence and requests for materials should be addressed to W.L.

Reprints and permission information is available at <http://www.nature.com/reprints>

Publisher's note Springer Nature remains neutral with regard to jurisdictional claims in published maps and institutional affiliations.



Open Access This article is licensed under a Creative Commons Attribution 4.0 International License, which permits use, sharing, adaptation, distribution and reproduction in any medium or format, as long as you give appropriate credit to the original author(s) and the source, provide a link to the Creative Commons license, and indicate if changes were made. The images or other third party material in this article are included in the article's Creative Commons license, unless indicated otherwise in a credit line to the material. If material is not included in the article's Creative Commons license and your intended use is not permitted by statutory regulation or exceeds the permitted use, you will need to obtain permission directly from the copyright holder. To view a copy of this license, visit <http://creativecommons.org/licenses/by/4.0/>.

© The Author(s) 2019